

## Quantitative two-photon imaging of blood flow in cortex

Jonathan D. Driscoll<sup>1</sup>, Andy Y. Shih<sup>1</sup>, Patrick J. Drew<sup>1</sup>, Ilya Valmianski<sup>1</sup> and David Kleinfeld<sup>1,2</sup>

<sup>1</sup> Department of Physics, University of California at San Diego, California 92093

<sup>2</sup> Graduate Program in Neurosciences, University of California at San Diego, California 92093

Prepared for: Imaging in Neuroscience and Development, Rafael Yuste, series Editor. Book 2: Optical Imaging in Neuroscience, F. Helmchen and A. Konnerth, editors, 2009, Cold Spring Harbor Laboratory Press, NY, Chapter 86

Abstract: 250 words  
Narrative: 2750 words  
Figures: 2 – both two column width and in color  
Figure captions: 520 words  
References: 24 for 750 words

Correspondence: David Kleinfeld  
Department of Physics  
University of California at San Diego  
9500 Gilman Drive  
La Jolla, CA 92093-0374  
Office: 858-822-0342  
Fax: 858-534-7697  
Email: [dk@physics.ucsd.edu](mailto:dk@physics.ucsd.edu)

## **Abstract**

**Cerebral blood flow plays a central role in maintaining homeostasis in the brain, and its dysfunction leads pathological conditions such as stroke. Moreover, understanding the dynamics of blood flow is central to the interpretation of data from imaging modalities, such as intrinsic optical signaling and functional magnetic resonance imaging, that rely on changes in cerebral blood flow and oxygen level to infer changes in the underlying neural activity. Recent advances in imaging techniques have allowed detailed studies of blood flow *in vivo* at high spatial and temporal resolutions. We discuss techniques to accurately measure cerebral blood flow at the level of individual blood vessels using two-photon laser-scanning microscopy. By directing the scanning laser along a user-defined path, it is possible to measure red blood cell velocity, as well as vessel diameter, across multiple vessels near simultaneously. The combination of these measurements allows accurate assessment of total flux with sufficient time resolution to measure fast modulations in flux, such as those caused by heart-beat, as well as slower signals caused by vasomotion and hemodynamic responses to stimulus.**

## **Introduction**

Neural activity is accompanied by both increases and decreases in local blood flow to active brain regions (Woolsey et al. 1996; Derdikman et al. 2003; Devor et al. 2008). Detection of function changes in cerebral blood flow are the basis of wide-field brain imaging modalities, including intrinsic optical signaling (Grinvald et al. 1986; Frostig et al. 1990) and functional magnetic resonance imaging (Ogawa et al. 1990). An understanding of the fundamental mechanisms of neurovascular coupling is critical for interpreting such data and is an active area of research.

Two-photon laser scanning microscopy (TPSLM) is an ideal method for studying blood in individual vessels, from the level of the pial vessels down to

subsurface capillaries. Two-photon microscopy has been used to acquire red blood cell (RBC) velocity (Kleinfeld et al. 1998; Belayev et al. 2002; Chaigneau et al. 2003; Hirase et al. 2004; Chuquet et al. 2007; Zhang and Murphy 2007) or lumen diameter (Takano et al. 2006; Devor et al. 2007; Devor et al. 2008; Shih et al. 2009) from a single vessel in a given imaging trial. However, the oxygen and nutrient carrying capacity of a vessel is proportional to its flux, which requires knowledge of both RBC velocity and vessel diameter. Since these two parameters can change independently, both must be measured simultaneously to accurately access total blood flow (Kontos 1989; Shih et al. 2009).

Here, we review general techniques for animal preparation and measurement of blood flow with TPSLM. We incorporate extensions to existing methods to accurately acquire flux data simultaneously across multiple vessels in a single trial. Central to these measurements is the ability to generate scan paths that smoothly connect user-defined lines of interest while maintaining high accuracy of the scan path.

## **MATERIALS**

### ***Reagents***

- Agarose, low melting point (Type III-A; Sigma)
- Dextrose, 5 % (w/v) in saline
- Fluorescein-dextran (2 MDa, Sigma) or Texas Red-dextran (70 kDa, Invitrogen), 5 % (w/v) in saline
- Heparin, 20 U/mL in saline
- Isoflurane (survival studies)
- Lidocaine solution, 2 % (v/v)
- Ophthalmic ointment

- Modified artificial cerebral spinal fluid (mACSF), free of carbonate and phosphate (125 mM NaCl, 10 mM glucose, 10 mM HEPES, 3.1 mM CaCl<sub>2</sub>, 1.3 mM MgCl<sub>2</sub>, pH 7.4) (Kleinfeld, 1996)
- Urethane or  $\alpha$ -chloralose (terminal studies)
- Note: prepared dextran-conjugated dye solutions can be frozen in aliquots at -20°C for later use.

### ***Disposables***

- Catheter, for tail-vein (Surflo; Terumo)
- Cover Glass, no. 1 thickness
- Dental acrylic (Grip Cement; Dentsply)
- Drill burrs, ½ and ¼ mm tips sizes (Henry Schein)
- Kimwipes
- Ophthalmic ointment
- PE-50 tubing, for femoral artery/vein catheter (Intramedic)
- Scalpel blades
- Screws, self-tapping (#000-3/32; Small Parts Inc.)
- SurgiFoam™ (Edgepark)
- Syringe needle (26 gauge)
- VetBond™ (3M)

### ***Surgical equipment***

- Blood gas monitor (RapidLab 248; Bayer)
- Blood pressure monitor (BP1, World Precision Instruments for intra-arterial; XBP1000, Kent Scientific for tail cuff measurements)
- Dental drill, air powered (Silent Air)
- Forceps, extra sharp (Dumont no. 55; Fine Science Tools)

- Glass cutter
- Head-frame, custom-made (Fig. 1A)
- Heat pad, feedback regulated (Harvard for rats; FHC for mice)
- Hemostats
- Isoflurane vaporizer (IsoTec)
- Periosteal elevator (Roboz)
- Pulse oximeter (Nonin for rats; Starr Life Sciences for mice)
- Screwdriver, miniature
- Stereotaxic frame (Kopf)

### ***Imaging equipment***

- Two-photon laser-scanning microscope; ours is a custom-design optimized for *in vivo* studies (Nguyen et al. 2006; 2009; Tsai and Kleinfeld 2009).
- Optical breadboard with head holder (Fig. 1B) and devices for physiological support and monitoring.

## **Procedures**

### ***1.) Surgical preparation for rat:***

- a. Common anesthetic choices include: (1) Urethane delivered intraperitoneally, *i.e.*, 1000 mg per kg rat initial dose with 100 mg per kg supplements as required (Kleinfeld and Denk 2000), or (2) Initial isoflurane for surgery followed by a transition to intravenous delivery of  $\alpha$ -chloralose for imaging, *i.e.*, an initial bolus at 50 mg per kg for induction and continuous delivery of 40 mg per kg for maintenance (Devor et al. 2007). Note that both urethane and  $\alpha$ -chloralose should be prepared fresh on the day of the experiment.

Heating to ~ 60°C and agitation is necessary to dissolve  $\alpha$ -chloralose.

- b. Check for lack of toe pinch reflex to ensure an adequate level of anesthesia.
- c. Secure animal in stereotaxic frame.
- d. Apply ophthalmic ointment to eyes to retain moisture.
- e. Inject 0.1 mL of 2 % (v/v) Lidocaine™ into the scalp subcutaneously before incision for local anesthesia.

**2.) Throughout surgery and imaging:**

- a. Ensure heart and breathing rates are within a normal range, *i.e.*, 300 to 400 and 60 to 120 events per minute, respectively, using a pulse oximeter.
- b. Maintain body temperature at 37°C using a feedback regulated rectal probe and heat pad.
- c. Inject 5 % (w/v) dextrose in saline intraperitoneally, 3 mL per kg rodent every 2 hours to maintain body fluids and energy requirements.
- d. Install a femoral artery and vein catheter to allow blood samples to be collected and various drugs to be administered, respectively. Monitored blood gas once every 2 hours.
- e. Monitor arterial blood pressure continuously from the femoral arterial line. Alternatively, the tail cuff method can be used to non-invasively measure blood pressure at intermittent time-points.

**3.) Cranial window surgery:**

- a. Shave and make a 4-5 cm incision down the midline of the scalp. Use a periosteal elevator to remove the thin periosteum from the surface of the skull.

- b. Demarcate the location of the cranial window. We typically consider measurements over primary somatosensory cortex, which is the part of parietal cortex that nominally lies between -1 and -5 mm relative to the Bregma point and between 1 and 7 mm from the midline on the medial-lateral axis for rats (Paxinos and Watson 1986).
- c. Attach a custom metal frame to the skull with dental acrylic. The frame rigidly holds the head of the animal to the optical apparatus (Figs. 1A and 1B). To achieve a reliable connection between acrylic and bone, the contact regions on the bone are cleaned of soft tissue, a thin layer of VetBond™ is applied, small self-tapping screws are introduced to the anterior and posterior aspects of the skull, and the screws, one of which passes through an opening in the frame, are then mechanically linked to the frame with dental cement (Fig. 1C). Secure the threads of the screw to the bone with a small dab of VetBond™. Note that the temporalis muscle may need to be retracted in some cases, and the temporal ridge flattened with a dental drill. This is to ensure that the metal head frame is cemented tangential to the cortical surface when imaging the lateral aspects of the barrel cortex.
- d. Generate a craniotomy above the brain region of interest using a high-speed drill. First thin the skull throughout the entire window to approximately one quarter of its original thickness using a ½ mm drill burr until the underlying pial vasculature becomes visible after application of mACSF. Flush the window regularly with mACSF during drilling to reduce heat buildup and to remove blood. Next, carefully thin the edges of the window with a ¼ mm burr until the bone begins to craze. Use a pair of forceps to gently separate the bone flap from the skull without protruding too deeply. Use two forceps to grasp adjacent corners of the loosened bone flap, and slowly peel it away from the underlying dura mater.

- e. Reflect the dura to the edges of the window (Fig. 1D). First generate a small incision using the cutting edge of a 26 gauge syringe needle. Bend the needle to an obtuse angle with hemostats to ensure the cutting edge approaches the dura at a suitable angle. Use two sharp no. 55 forceps to gently lift the dura away from the cortical surface, starting at the incision site, and tearing in small increments. Whenever possible, tear around large dural vessels to avoid bleeding. Limit any dural bleeding with small pieces of Surgifoam™ soaked in mACSF and KimWipes™, twisted to a fine point with the fingers. The cranial window is kept moist with a piece of moist Surgifoam™. Retract the dural flaps to the side of the window, and the cortical surface is flushed with mACSF. It is crucial to avoid any damage to pial vessels. Hemorrhaging will alter cerebral blood flow, accelerate edema, and severely degrade imaging quality.
- f. Fill the interior of the chamber with 1.5 % (w/v) low melting point agarose dissolved in mACSF (Fig. 1D) (Kleinfeld and Delaney 1996). Dissolve the agarose by heating in a microwave. The temperature of the agarose must not exceed 37°C before it is applied to the brain.
- g. Immediately seal the chamber using a cover glass as a window (Fig. 1D). Resealing the craniotomy is crucial to protect the cortex and suppress motion from cranial-pressure fluctuations due to heart beat and breathing. An edge of the window can remain uncovered to allow insertion of electrodes or micropipettes.
- h. Suture the skin together around the frame, and trail agarose around the cover glass to hold water for the dipping lens.
- i. Stabilize the animals on an optical breadboard for imaging, using the frame as a head support. Our separate plate can be transported

between surgical and imaging suites with the animal and all physiological monitoring devices assembled as one unit (Fig. 1B).

## Example Application

A cranial window was generated over the rat somatosensory cortex (Fig. 2). Intrinsic optical imaging was used to determine the locations of the hindlimb and forelimb cortical representation (Drew and Feldman 2009). The cerebral vasculature of the hindlimb somatosensory region was mapped using a TPLSM image stack obtained with a low magnification 4X objective (Fig. 2A). A single penetrating arteriole and neighboring ascending venule were selected for measurement under a 40X objective (Fig. 2B).

A scan path was created to traverse along the length of the lumen center, and across the lumen width for each vessel. The accuracy of the scan path can be verified by comparing the value of the mirror position encoder with the control voltage. Scan accuracy in user-selected linear scan paths is around 1  $\mu\text{m}$ , while intervening segments which connect the user defined regions and are not used in data analysis have a higher error, up to about 5  $\mu\text{m}$  (Fig. 2C). The resulting linescan is a space-time image (Fig. 2D).

Portions of the scan path along the vessel length appear as streaks within the line-scan image. These streaks represent non-fluorescent RBCs that move through a fluorescent background. The x-axis represents the distance traveled by the RBCs, and the y-axis is the time. The centerline velocity is then calculated from the slope of the RBC streaks (Fig. 2E, right panel). Previously, singular value decomposition was used to find the slope of these streaks and calculate the RBC velocity (Kleinfeld et al. 1998; Schaffer et al. 2006). A faster method that can calculate the velocity in near real time makes use of the Radon transform (Drew et al. 2009). In either case, the velocity is taken using windowed portions of the linescans, typically 25 ms of data for a Nyquist frequency of 20 Hz (see figure 1 in Chapter 7). This is sufficient to capture the fastest biological signal, the heart rate, without aliasing the second harmonic of the rate.

Portions of the scan path across the vessel width capture the diameter of the vascular lumen, since the fluorescently labeled blood plasma provides high contrast with the unlabeled region immediately outside the vessel. To increase the signal-to-noise ratio, multiple scans across the vessel diameter are averaged together before the profile is calculated. As with the velocity calculation, the diameter transform is taken on a windowed portion of the data. Typically, the same window size as for velocity is used so that both parameters can be calculated on the same time scale.

Vessel diameter is calculated as full-width at half-max (FWHM) of the vessel profile (Fig. 2E, left). Since the intensity profile tends decrease in the center of the vessel, where a large volume of RBCs exclude the fluorescently labeled plasma, the two outermost half-max points are used. Linear interpolation is used to add subpixel accuracy to the diameter measurement.

We now consider combining the velocity and diameter measurements to calculate flux. In laminar flow, the velocity  $\mathbf{v}(\mathbf{r})$  of the fluid through the pipe with radius  $\mathbf{R}$  measured at a distance  $r$  from the center has a quadratic profile, with a maximal velocity  $\mathbf{v}(\mathbf{0})$  in the center and tapering to zero at the edges, *i.e.*,

$$(1) \quad \mathbf{v}(\mathbf{r}) = \mathbf{v}(\mathbf{0}) \left( 1 - \frac{r^2}{R^2} \right).$$

Measurements of RBC velocity as a function of distance from the vessel center show that this model is a close approximation (Schaffer et al. 2006), although systematic deviations result from the non-negligible size of the RBCs. This tends to flatten the profile, and prevents the velocity from reaching zero at the edges of the vessel. Neglecting these effects, the integrated flux through the vessel is given by (Helmchen and Kleinfeld 2008):

$$(2) \quad F = \frac{1}{2} \mathbf{v}(\mathbf{0}) \pi R^2.$$

In our example, both vessel diameter and RBC velocity in the arteriole respond to somatotopic stimulation. The flux through the arteriole increases by

approximately 100 % over baseline, compared with 35 % and 40 % for diameter and velocity measurements alone, respectively (Fig. 2F). Since the scan path runs at 733 Hz in this example, the diameter and RBC velocity traces are collected near simultaneously from both the penetrating arteriole and ascending venule.

## Generation of Spatially Optimized Line Scans

The scanning laser of the microscope is directed by a pair of fast X-Y scan mirrors (Cambridge Technology, 6210H galvanometer optical scanner with MicroMax 673xx dual-axis servo driver). The mirror controller employs a closed loop position feedback system to accurately map control voltage to mirror position. The position accurately tracks the control voltage, with  $\sim 90 \mu\text{s}$  delay.

To create an arbitrary scanning path, several full-frame images of the region containing the desired vessels are first acquired, and averaged together to increase signal to noise. This image is loaded by a custom software written in MATLAB™ (MathWorks), which allows users to interactively create lines of interest, *i.e.*, scans across or along vessels, on the full frame image.

The mirror voltages used to acquire the original full frame image are known, so that positions on the image can be mapped one-to-one to mirror voltages. Linear portions of the scan path, such as those used to track along a vessel to measure RBC speed and those that span the vessel to measure diameter, are given by

$$(3) \quad \vec{\mathbf{P}} = \vec{\mathbf{P}}_0 + \vec{\mathbf{V}}_{linear} \cdot t$$

where  $\vec{\mathbf{P}}$  and  $\vec{\mathbf{V}}$  are two dimensional vectors that contain X and Y coordinates.

Linear portions of the scan path, scanned at constant velocity, must be connected by a function that creates a physically realistic path for the mirrors to follow (Lillisa et al. 2008). Although there are an arbitrary number of such functions, the simplest is a third-order polynomial given by

$$(4) \quad \vec{\mathbf{P}}_{spline} = \vec{\mathbf{P}}_i + \vec{\mathbf{V}}_i \cdot \mathbf{t} + \vec{\mathbf{C}} \cdot \mathbf{t}^2 + \vec{\mathbf{D}} \cdot \mathbf{t}^3 .$$

For computational convenience, the connecting spline is taken to start at  $\mathbf{t} = 0$ , and end at  $\mathbf{t} = \tau$ . The initial position  $\vec{\mathbf{P}}_i$  and velocity  $\vec{\mathbf{V}}_i$  of the spline are set to match the position and velocity of the end of the linear region preceding the spline.

The additional spline parameters depend on the length (in time) of the spline,  $\tau$ , and the final position and velocity of the spline, and are given by

$$(5) \quad \mathbf{C} = \frac{3\mathbf{P}_f}{\tau^2} - \frac{3\mathbf{P}_i}{\tau^2} - \frac{2\mathbf{V}_i}{\tau} - \frac{\mathbf{V}_f}{\tau}$$

and

$$(6) \quad \mathbf{D} = \frac{\mathbf{V}_f}{3\tau^2} - \frac{\mathbf{V}_i}{3\tau^2} - \frac{2\mathbf{C}}{3\tau}$$

The value of  $\tau$  used should be the smallest positive real value which does not subject the mirrors to an acceleration larger than a user defined maximal value,  $\mathbf{m}$ , typically 100 V/ms<sup>2</sup>. Since the acceleration of the spline is a linear function of time, the extreme values of acceleration occur at the beginning and the end of the spline.

Candidate values for the shortest possible spline length are found by setting the mirror acceleration to  $\pm\mathbf{m}$  at the beginning at end of spline, and finding all positive real values for  $\tau$ :

$$(7) \quad \mathbf{0} = \pm\mathbf{m} \tau^2 + (4\vec{\mathbf{V}}_f + 2\vec{\mathbf{V}}_i)\tau + (6\vec{\mathbf{P}}_i - 6\vec{\mathbf{P}}_f) \quad (\text{acceleration of at start of spline})$$

$$(8) \quad \mathbf{0} = \pm\mathbf{m} \tau^2 + (4\vec{\mathbf{V}}_i + 2\vec{\mathbf{V}}_f)\tau + (6\vec{\mathbf{P}}_i - 6\vec{\mathbf{P}}_f) \quad (\text{acceleration of at end of spline})$$

The actual time used is the smallest value that keeps the acceleration within limits at the beginning and end of the spline, i.e., all of  $|2\mathbf{C}_x| < \mathbf{m}$ ,  $|2\mathbf{C}_y| < \mathbf{m}$ ,  $|2\mathbf{C}_x + 6\mathbf{D}_x\tau| < \mathbf{m}$ , and  $|2\mathbf{C}_y + 6\mathbf{D}_y\tau| < \mathbf{m}$  are true.

## Epilog

Two photon scanning microscopy offers a means to obtain high-resolution images of RBC velocity and vessel diameter *in vivo*. These measurements can be combined to calculate the flux for a given vessel, which is a more accurate metric of the oxygen and nutrient carrying capability of blood.

Velocity and diameter measurements can change independently (Fig. 2F) and thus they must be measured near-simultaneously to accurately access flux. This can be achieved with the spatially optimized linescan algorithm described above. This technique can be extended to image other types of fluorescent signals, for instance, neural activity as indicated by calcium sensitive dyes. In principle, this technique can be readily extended to scan in three dimensions as well. However, the speed of current mechanical Z-axis scanners is currently much slower than what can be achieved when scanning in the X-Y plane alone (Gobel and Helmchen 2007; Göbel et al. 2007).

## Acknowledgements

We thank Quoc-Thang Nguyen for useful discussions on MPScope scan software. This work was funded by the NIH (grants EB003832, NS059832, and RR021907 to DK and AG029681 to Gert Cauwenberghs), the NSF (grant DBI 0455027), and a postdoctoral fellowship from the American Heart Association to AYS.

## References

- Belayev, L., Pinard, E., Nallet, H., Seylaz, J., Liu, Y., Riyamongkol, P., Zhao, W., Busto, R., and Ginsberg, M.D. 2002. Albumin therapy of transient focal cerebral ischemia: *In vivo* analysis of dynamic microvascular responses. *Stroke* **33**: 1077-1084.
- Chaigneau, E., Oheim, M., Audinat, E., and Charpak, S. 2003. Two-photon imaging of capillary blood flow in olfactory bulb glomeruli. *Proceedings of the National Academy of Sciences USA* **100**: 13081-13086.
- Chuquet, J., Hollender, L., and Nimchinsky, E.A. 2007. High-resolution *in vivo* imaging of the neurovascular unit during spreading depression. *Journal of Neuroscience* **27**: 4036-4044.
- Derdikman, D., Hildesheim, R., Ahissar, E., Arieli, A., and Grinvald, A. 2003. Imaging spatiotemporal dynamics of surround inhibition in the barrels somatosensory cortex. *Journal of Neuroscience* **23**: 3100-3105.
- Devor, A., Hillman, E.M., Tian, P., Waeber, C., Teng, I.C., Ruvinskaya, L., Shalinsky, M.H., Zhu, H., Haslinger, R.H., Narayanan, S.N. et al. 2008. Stimulus-induced changes in blood flow and 2-deoxyglucose uptake dissociate in ipsilateral somatosensory cortex. *Journal of Neuroscience* **28**: 14347-14357.
- Devor, A., Tian, P., Nishimura, N., Teng, I.C., Hillman, E.M., Narayanan, S.N., Ulbert, I., Boas, D.A., Kleinfeld, D., and Dale, A.M. 2007. Suppressed neuronal activity and concurrent arteriolar vasoconstriction may explain negative blood oxygenation level-dependent signaling. *Journal of Neuroscience* **27**: 4452-4459.
- Drew, P.J. and Feldman, D.E. 2009. Intrinsic signal imaging of deprivation-induced contraction of whisker representations in rat somatosensory cortex. *Cerebral Cortex* **19**: 331-348.
- Drew, P.J., P., B., Cauwenberghs, G., Shih, A.Y., and Kleinfeld, D. 2009. Rapid determination of particle velocity from space-time images using the Radon transform. *Journal of Computational Neuroscience* **Epub ahead of print**.
- Frostig, R.D., Lieke, E.E., Ts'o, D.Y., and Grinvald, A. 1990. Cortical functional architecture and local coupling between neuronal activity and the microcirculation revealed by *in vivo* high-resolution optical imaging of intrinsic signals. *Proceedings of the National Academy of Sciences USA* **87**: 6082-6086.
- Gobel, W. and Helmchen, F. 2007. New angles on neuronal dendrites *in vivo*. *Journal of Neurophysiology* **in press**.
- Göbel, W., Kampa, B.M., and Helmchen, F. 2007. Imaging cellular network dynamics in three dimensions using fast 3D laser scanning. *Nature Methods* **4**: 73-79.
- Grinvald, A., Lieke, E.E., Frostig, R.D., Gilbert, C.D., and Wiesel, T.N. 1986. Functional architecture of cortex revealed by optical imaging of intrinsic signals. *Nature* **324**: 361-364.
- Helmchen, F. and Kleinfeld, D. 2008. *In vivo* measurements of blood flow and glial cell function with two-photon laser scanning microscopy. *Methods in Enzymology* **444**: 231-254.
- Hirase, H., Creso, J., and Buzsaki, G. 2004. Capillary level imaging of local cerebral blood flow in bicuculline-induced epileptic foci. *Neuroscience* **128**: 209-216.

- Kleinfeld, D. and Delaney, K.R. 1996. Distributed representation of vibrissa movement in the upper layers of somatosensory cortex revealed with voltage sensitive dyes. *Journal of Comparative Neurology* **375**: 89-108.
- Kleinfeld, D. and Denk, W. 2000. Two-photon imaging of neocortical microcirculation. in *Imaging Neurons: A Laboratory Manual* (ed. R. Yuste, F. Lanni, and A. Konnerth), pp. 23.21-23.15. Cold Spring Harbor Laboratory Press, Cold Spring Harbor.
- Kleinfeld, D., Mitra, P.P., Helmchen, F., and Denk, W. 1998. Fluctuations and stimulus-induced changes in blood flow observed in individual capillaries in layers 2 through 4 of rat neocortex. *Proceedings of the National Academy of Sciences USA* **95**: 15741-15746.
- Kontos, H.A. 1989. Validity of cerebral arterial blood flow calculations from velocity measurements. *Stroke* **20**: 1-3.
- Lillisa, K.P., Enga, S., and Whitea, J.A. 2008. Two-photon imaging of spatially extended neuronal network dynamics with high temporal resolution. *Journal of Neuroscience Methods* **172**: 178-184.
- Nguyen, Q.-T., Dolnick, E.M., Driscoll, J., and Kleinfeld, D. 2009. MPScope 2.0: A computer system for two-photon laser scanning microscopy with concurrent plasma-mediated ablation and electrophysiology. in *Methods for In Vivo Optical Imaging, 2nd edition* (ed. R.D. Frostig), pp. 117-142. CRC Press, Boca Raton.
- Nguyen, Q.-T., Tsai, P.S., and Kleinfeld, D. 2006. MPScope: A versatile software suite for multiphoton microscopy. *Journal of Neuroscience Methods* **156**: 351-359.
- Ogawa, S., Lee, T.M., Kay, A.R., and Tank, D.W. 1990. Brain magnetic resonance imaging with contrast dependent on blood oxygenation. *Proceedings of the National Academy of Sciences USA* **87**: 9868-9872.
- Paxinos, G. and Watson, C. 1986. *The Rat Brain in Stereotaxic Coordinates*. Academic Press, San Diego.
- Schaffer, C.B., Friedman, B., Nishimura, N., Schroeder, L.F., Tsai, P.S., Ebner, F.F., Lyden, P.D., and Kleinfeld, D. 2006. Two-photon imaging of cortical surface microvessels reveals a robust redistribution in blood flow after vascular occlusion. *Public Library of Science Biology* **4**: 258-270.
- Shih, A.Y., Friedman, B., Drew, P.J., Tsai, P.S., Lyden, P.D., and Kleinfeld, D. 2009. Active dilation of penetrating arterioles restores red blood cell flux to penumbral neocortex after focal stroke. *Journal of Cerebral Blood Flow and Metabolism* **29**: 738-751.
- Takano, T., Tian, G.F., Peng, W., Lou, N., Libionka, W., Han, X., and Nedergaard, M. 2006. Astrocyte-mediated control of cerebral blood flow. *Nature Neuroscience* **9**: 260-267.
- Tsai, P.S. and Kleinfeld, D. 2009. In vivo two-photon laser scanning microscopy with concurrent plasma-mediated ablation: Principles and hardware realization. in *Methods for In Vivo Optical Imaging, 2nd edition* (ed. R.D. Frostig), pp. 59-115. CRC Press, Boca Raton.
- Woolsey, T.A., Rovainen, C.M., Cox, S.B., Henger, M.H., Liange, G.E., Liu, D., Moskalenko, Y.E., Sui, J., and Wei, L. 1996. Neuronal units linked to microvascular modules in cerebral cortex: Response elements for imaging the brain. *Cerebral Cortex* **6**: 647-660.

Zhang, S. and Murphy, T.H. 2007. Imaging the impact of cortical microcirculation on synaptic structure and sensory-evoked hemodynamic responses in vivo. *Public Library of Science Biology* 5: e119.

## Figure Legends

**Figure 1. Set-up for in vivo imaging of blood flow through a cranial window. (A)** To immobilize the head of the animal during imaging, we designed a metal frame that could be cemented to the skull, and then anchored to an optical set-up. The frame is constructed of type 410 stainless steel with dimensions of 2.00 in long, 0.61 in wide and 0.029 in thick, and can be secured between two posts in a standard optical breadboard. An inset region, 0.015 in deep, borders the frame window to hold a cover glass over the craniotomy. The window cover, 0.015 in thick of type 301 stainless steel, is then secured to the frame with four screws, sandwiching a no. 1 cover glass in place. **(B)** A typical experimental set-up. The metal frame attached to the skull is immobilized between two anchoring posts inserted into an optical breadboard. Rat skull diagram in panel B adapted from Paxinos and Watson (Paxinos and Watson 1986). **(C)** Diagram of cranial window preparation for rat. **(D)** A cross-sectional view of the cranial window. The inset diagram shows an inverted coronal view of surface vessels and deep microvessels.

**Figure 2. Simultaneous measurement of diameter and velocity in multiple vessels using spatially optimized line scans. (A)** Image of fluorescently stained vessels in somatosensory cortex of a Sprague Dawley rat. The forelimb and hindlimb representations across cortex were mapped using intrinsic optical imaging. **(B)** Image of a surface arteriole and venule, with user-defined scan path superimposed. Portions of the scan path along the length are used to calculate RBC velocity, while portions across the diameter of the vessels are used to calculate diameter. Scans were acquired at a rate of 735 lines per second. **(C)** Image of scan path, colored to show the error between the desired scan path and the actual path the mirrors traversed. The error along linear portions of the image is about 1  $\mu\text{m}$ , and increases when the mirrors undergo rapid acceleration. The error between successive scans of the same path is less than 0.15  $\mu\text{m}$ , several times lower than the point-spread function of a TPLSM. **(D)** Mirror speed as a function of time. Note that portions used to acquire diameter and velocity data are constant speed (top). The line-scans generated from the path can be stacked sequentially as a function of time to produce a raw cascade image (bottom). **(E)** Vessel diameter is calculated as the full-width half-maximum of a time-average of several scans across the width of a vessel (left). Red blood cell velocity is calculated from the angle of the RBC streaks. **(F)** Data traces of diameter, velocity, and flux for the arteriole and

venule, processed to remove heart rate and smoothed with a running window. Both vessels show an increase in flux in response to forelimb stimulation. In the arteriole, this flux increase is due to simultaneous increase of lumen diameter and RBC velocity. In contrast, flux increase in the venule is due only to an increase in RBC velocity, as diameter is unchanged by stimulation.

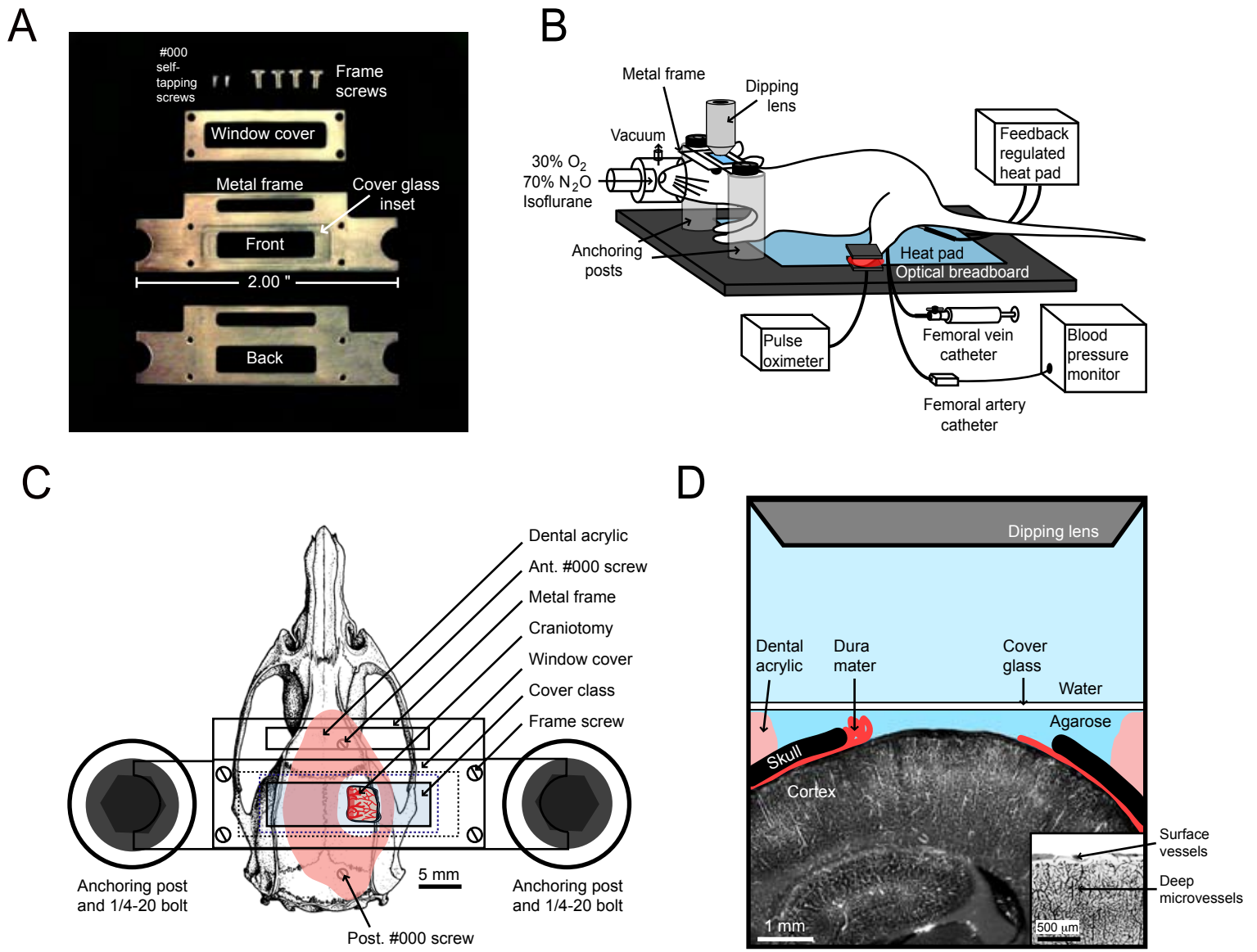


Figure 1. Driscoll et al.

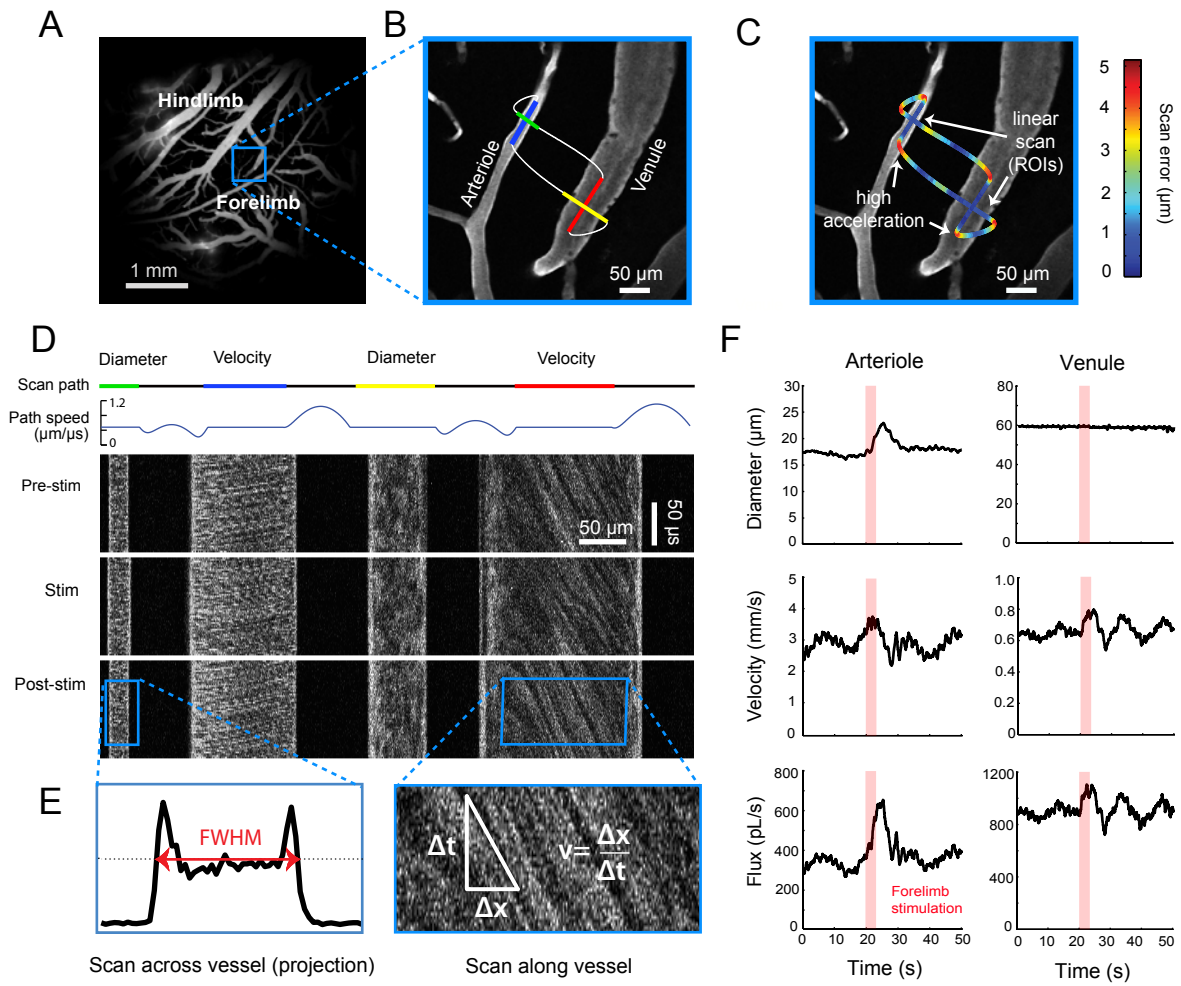


Figure 2. Driscoll et al.